



Relationship Between Reactive Astrocytes, by [¹⁸F]SMBT-1 Imaging, with Amyloid-Beta, Tau, Glucose Metabolism, and TSPO in Mouse Models of Alzheimer's Disease

Yanyan Kong¹ · Cinzia A. Maschio^{2,4} · Xuefeng Shi³ · Fang Xie¹ · Chuantao Zuo¹ · Uwe Konietzko² · Kuangyu Shi⁵ · Axel Rominger⁵ · Jianfei Xiao¹ · Qi Huang¹ · Roger M. Nitsch² · Yihui Guan¹ · Ruiqing Ni^{2,4,5,6} 

Received: 25 September 2023 / Accepted: 6 March 2024
© The Author(s) 2024

Abstract

Reactive astrocytes play an important role in the development of Alzheimer's disease (AD). Here, we aimed to investigate the temporospatial relationships among monoamine oxidase-B, tau and amyloid- β (A β), translocator protein, and glucose metabolism by using multitracer imaging in AD transgenic mouse models. Positron emission tomography (PET) imaging with [¹⁸F]SMBT-1 (monoamine oxidase-B), [¹⁸F]florbetapir (A β), [¹⁸F]PM-PBB3 (tau), [¹⁸F]fluorodeoxyglucose (FDG), and [¹⁸F]DPA-714 (translocator protein) was carried out in 5- and 10-month-old APP/PS1, 11-month-old 3 \times Tg mice, and age-matched wild-type mice. The brain regional referenced standard uptake value (SUVR) was computed with the cerebellum as the reference region. Immunofluorescence staining was performed on mouse brain tissue slices. [¹⁸F]SMBT-1 and [¹⁸F]florbetapir SUVRs were greater in the cortex and hippocampus of 10-month-old APP/PS1 mice than in those of 5-month-old APP/PS1 mice and wild-type mice. No significant difference in the regional [¹⁸F]FDG or [¹⁸F]DPA-714 SUVRs was observed in the brains of 5- or 10-month-old APP/PS1 mice or wild-type mice. No significant difference in the SUVRs of any tracer was observed between 11-month-old 3 \times Tg mice and age-matched wild-type mice. A positive correlation between the SUVRs of [¹⁸F]florbetapir and [¹⁸F]DPA-714 in the cortex and hippocampus was observed among the transgenic mice. Immunostaining validated the distribution of MAO-B and limited A β and tau pathology in 11-month-old 3 \times Tg mice; and A β deposits in brain tissue from 10-month-old APP/PS1 mice. In summary, these findings provide in vivo evidence that an increase in astrocyte [¹⁸F]SMBT-1 accompanies A β accumulation in APP/PS1 models of AD amyloidosis.

Keywords Alzheimer's disease · Amyloid-beta · Glia · MAO-B · PET · Tau · TSPO

Introduction

Alzheimer's disease (AD) is pathologically characterized by abnormal accumulation of amyloid-beta (Ab), tau tangles, reactive astrocytes, microgliosis, and neuronal loss. Astrocytes are the most abundant glial cell population in the brain and play an important role in maintaining synaptic homeostasis by regulating synapse function, calcium signalling, and brain metabolism [80]. Reactive astrocytes are involved early in the pathophysiology of AD and have a dynamic profile during disease progression [6, 23]. Post-mortem studies of AD brains have demonstrated abundant reactive astrocytes and microglia around A β plaques and tangles [51, 57, 71]. Previous topological analyses revealed that astrocytes respond to plaque-induced neurological injury primarily by changing their phenotype and hence function rather than their location [28]. The heterogeneity

✉ Yihui Guan
guanyihui@hotmail.com

✉ Ruiqing Ni
ruiqing.ni@uzh.ch

¹ PET Center, Huashan Hospital, Fudan University, Shanghai, China

² Institute for Regenerative Medicine, University of Zurich, Zurich, Switzerland

³ Qinghai Provincial People's Hospital, Xining, China

⁴ Zurich Neuroscience Zentrum (ZNZ), Zurich, Switzerland

⁵ Department of Nuclear Medicine, Inselspital, University of Bern, Bern, Switzerland

⁶ Institute for Biomedical Engineering, University of Zurich & ETH Zurich, Zurich, Switzerland

of astrocyte and microglial profiles in these models has been documented in earlier transcriptomic studies. Reactive astrocytes with altered metabolism and function have been demonstrated in an amyloidosis animal model [2]. Reactive astrocytes acquire neuroprotective and deleterious signatures in response to tau and A β pathology [36] and influence the effects of amyloid- β on tau pathology in preclinical AD [5]. Reactive astrocytes, as measured by cerebrospinal fluid (CSF) levels of glial fibrillary acidic protein (GFAP), have been shown to mediate the effect of A β on tau and drive downstream neurodegeneration and cognitive impairment in patients with AD [24] and preclinical AD. Monoamine oxidase B (MAO-B) is expressed mainly on astrocytes but also on serotonergic and histaminergic neurons. MAO-B reversibly increases astrocytic γ -aminobutyric acid (GABA) production in reactive astrocytes [37], which is associated with synaptic and memory impairments in APP/PS1 mice with amyloidosis [63]. Moreover, MAO-B mediates the aberrant synthesis of hydrogen peroxide (H₂O₂) in reactive astrocytes. There is an age-related increase in MAO-B expression in astrocytes [77]. Furthermore, the levels of MAO-B have been shown to increase in the brains of sporadic and autosomal dominant AD patients and mild cognitive impairment patients. A recent study showed that MAO-B is elevated in AD pyramidal neurons, is associated with γ -secretase, and regulates neuronal A β -peptide levels [70]. In APP/PS1 mice, upregulated levels of MAO-B and reactive astrocytes increase the number of tau inclusions, increase neuronal death and brain atrophy, and impair spatial memory in an H₂O₂-dependent manner [17]. Reactive astrocytes and MAO-B have thus emerged as potential treatment targets for AD [72].

Several positron emission tomography (PET) tracers for reactive astrocytes have been developed, including the irreversible MAO-B tracers [¹¹C]deuterium-L-deprenyl (DED) and [¹⁸F]F-DED [3, 60, 66], the reversible MAO-B tracer [¹⁸F]SMBT-1, the substrate-based MAO-B tracer [¹¹C]Cou [21], the mitochondrial imidazoline 2 binding site (I₂BS) tracer [¹¹C]BU99008 [24] and [¹¹C]acetate [53], and the thyroid hormone transporter OATP1C1 [¹⁸F]sulforhodamine-101 [45]. In vivo [¹¹C]DED has demonstrated divergent longitudinal changes in reactive astrocytes and

amyloid in patients with autosomal dominant [81] and prodromal AD [10, 67]. Increased brain [¹⁸F]SMBT-1 binding in A β + patients compared with that in A β -nondemented controls has been observed and is associated with A β accumulation at the preclinical stage of AD [13, 31, 82, 83]. Moderate correlations were found between [¹¹C]DED and [¹¹C]PIB and [¹⁸F]FDG [10, 69]. In animal models (APP-swe, PS2APP, APPArcSwe), reactive astrocytes measured by using [¹¹C]DED and [¹⁸F]F-DED precede the increase in the amyloid-PET signal [3, 60, 66]. Regional dependency of [¹⁸F]SMBT-1 and [¹¹C]DED binding has been reported in the human brain by PET in vivo and by autoradiography on postmortem brain tissue, with the highest uptake in the striatum and thalamus, followed by the hippocampus and cortical regions; white matter; and rather low uptake in the cerebellum [26, 29, 31]. Moreover, MAO-B is also particularly enriched in the superficial layer [77].

The aim of the current study was to evaluate the distribution of the novel tracer [¹⁸F]SMBT-1 in two mouse models of AD (APP/PS1, 3 \times Tg). We assessed the temporospatial relationship of astrocyte MAO-B with alterations in A β accumulation (by [¹⁸F]florbetapir), tau levels (by [¹⁸F]PM-PBB3, florzolotau, APN-1607), glucose metabolism (by [¹⁸F]fluorodeoxyglucose, FDG), and translocator protein (TSPO, by [¹⁸F]DPA-714) using a multitracer approach. We hypothesized that MAO-B increase (reactive astrocytes) is associated with A β accumulation in mouse model of amyloidosis.

Methods

Animal Models

The animal models used in the study are summarized in Table 1. 3 \times Tg mice [B6;129-Psen1tm1MpmTg(APPswe, tauP301L)1Lfa/Mmjax] aged 11 months [59], and APP/PS1 mice [B6. Cg-Tg(APPswe, PSEN1dE9)85Dbo/Mmjax] mice overexpressing the human APP695 transgene (Swedish (K670N/M671L)) and with PSEN1 mutations [34] aged 5 and 10 months were used (Jax Laboratory, USA). Wild-type C57BL6 mice were obtained from Charles River, Germany,

Table 1 Information on the animal models used in the study

Mice	Age (month)	[¹⁸ F]SMBT-1	[¹⁸ F]DPA-714	[¹⁸ F]PM-PBB3	[¹⁸ F]florbetapir	[¹⁸ F]FDG	[¹¹ C]PIB
APP/PS1	5	6 M	6 M	3 M	10 M	6 M	
	10	6 M	6 M	3 M	9 M	6 M	
3 \times Tg	11	8 M	3 M	5 M	3 M	3 M	2F/2 M
Wildtype	5	9 M	9 M	9 M	8 M	6 M	
	10	8 M	6 M	6 M	10 M	6 M	4 M

F, female; M, male

and Cavins Laboratory Animal Co., Ltd., of Changzhou. Mice were housed in ventilated cages inside a temperature-controlled room under a 12-h dark/light cycle. Pelleted food (3437PXL15, CARGILL) and water were provided ad libitum. Paper tissue and red Tecniplast Mouse House® (Tecniplast, Italy) shelters were placed in cages for environmental enrichment.

Radiosynthesis

[¹⁸F]SMBT-1 (0.74 GBq/ml) was radiosynthesized from its precursor according to previous methods [31]. [¹⁸F]DPA-714 (1.48 GBq/ml) was labelled with ¹⁸F at its 2-fluoroethyl moiety after nucleophilic substitution of the corresponding linear analog [32]. [¹⁸F]PM-PBB3 (1.48 GBq/ml) was synthesized from an automatic synthesis module and kit provided by APRINOIA therapeutics (Suzhou, China) [39, 44]. [¹⁸F]florbetapir (0.56 GBq/ml) was radiosynthesized from its precursor in a fully automated procedure suitable for routine clinical application [49]. [¹⁸F]FDG (1.48 GBq/ml) was prepared in the radiochemistry facility of the PET Center, Huashan Hospital, Fudan University, for clinical use under Good Manufacturing Practices requirements. [¹¹C]PIB (0.074 GBq/ml) was radiosynthesized according to a previously described protocol [86]. The identities of the aforementioned final products were confirmed by comparison with the high-performance liquid chromatography (HPLC) retention times of the nonradioactive reference compounds obtained by coinjection using a Luna 5 µm C18(2) 100 Å (250 mm × 4.6 mm) column (Phenomenex) with acetonitrile and water (60:40) as the solvent at a 1.0 mL/min flow rate. A radiochemical purity > 95% was achieved for all the aforementioned tracers. The HPLC and quality control (QC) data of [¹⁸F]SMBT-1 are shown in SFig. 1.

MicroPET

PET experiments using [¹⁸F]SMBT-1, [¹⁸F]florbetapir, [¹⁸F]PM-PBB3, [¹⁸F]FDG, and [¹⁸F]DPA-714 were sequentially performed using a Siemens Inveon PET/CT system (Siemens Medical Solutions, United States) [43]. There was two days of rest between each scan. To confirm the results of [¹⁸F]florbetapir imaging in 3×Tg mice, [¹¹C]PIB was also performed on four 3×Tg mice and four wild-type mice. Prior to the scans, the mice were anesthetized using isoflurane (1.5%) in medical oxygen (0.3–0.5 L/min) at room temperature with an isoflurane vaporizer (Molecular Imaging Products Company, USA). The mice were positioned in a spreadup position on the heated imaging bed and subjected to inhalation of the anesthetic during the PET/computed tomography (CT) procedure. The temperature of the mice was monitored. A single dose of tracer (~0.37 MBq/g body weight, 0.1–0.2 mL) was injected into the animals through the tail

vein under isoflurane anesthesia. For dynamic PET, the raw PET data were binned into nine frames (9 × 600 s) to obtain the time activity curve ([¹⁸F]SMBT-1 and [¹⁸F]PM-PBB3). Static PET/CT images were obtained for a 10-min period at specific times post intravenous administration, depending on the tracer used: [¹⁸F]FDG at 60–70 min, [¹⁸F]florbetapir at 50–60 min, [¹⁸F]SMBT-1 at 60–70 min, [¹⁸F]DPA-714 at 40–50 min, [¹⁸F]PM-PBB3 at 90–100 min, and [¹¹C]PIB at 50–60 min. PET/CT images were reconstructed using the ordered subsets expectation maximization 3D algorithm (OSEM3D), with a matrix size of 128 × 128 × 159 and a voxel size of 0.815 mm × 0.815 mm × 0.796 mm. The data were reviewed using Inveon Research Workplace software (Siemens). Attenuation corrections derived from hybrid CT data were applied.

PET Data Analysis

The images were processed and analyzed using PMOD 4.4 software (PMOD Technologies Ltd., Switzerland) by two people. Radioactivity is presented as the standardized uptake value (SUV) (decay-corrected radioactivity per cm³ divided by the injected dose per gram body weight). The time – activity curves were deduced from specific volumes of interest that were defined based on a mouse MRI T₂-weighted image template [81]. The brain regional SUVs were calculated using the cerebellum (Cb) as the reference region. The mask was applied for signals outside the brain volumes of interest for illustration.

Immunofluorescence Staining

Mice were perfused under ketamine/xylazine/acepromazine maleate anesthesia (75/10/2 mg/kg body weight, i.p. bolus injection) with ice-cold 0.1 M phosphate-buffered saline (PBS, pH 7.4) and 4% paraformaldehyde (PFA) in 0.1 M PBS (pH 7.4), fixed for 24 h in 4% PFA and then stored in 0.1 M PBS at 4 °C. The APPS/PS1 mice used for staining were subjected to in vivo imaging. The 3×Tg mice were purchased from the same source (Jax Laboratory) but different for in vivo and ex vivo experiments. Sagittal and coronal brain Sects. (40 mm) were cut around bregma 0 to -2 mm. The sections were first washed in PBS 3 × 10 min, followed by antigen retrieval for 20 min in citrate buffer at room temperature. Then, the sections were permeabilized and blocked in 5% normal donkey or goat serum and 1% Triton-PBS for one hour at room temperature. Free-floating tissue sections were incubated with primary antibodies against 6E10, complement component C3d (C3D), CD68, AT-8, GFAP, glucose transporter type-1 (Glut1), MAO-B overnight at 4 °C (Suppl. Table 1) [40] and with the appropriate secondary antibodies. The sections were incubated for 15 min in 4',6-diamidino-2-phenylindole (DAPI), washed

2 × 10 min with PBS, and mounted with VECTASHIELD Vibrance Antifade Mounting Media (Vector Laboratories, Z J0215). The brain sections were imaged at ×20 magnification using an Axio Observer Z1 slide scanner (Zeiss, Germany) using the same acquisition settings for all slices and at ×10 and ×63 magnification using a Leica SP8 confocal microscope (Leica, Germany). The images were analyzed by a person blinded to the genotype using Qupath and ImageJ (NIH, U.S.A.).

Statistics

Two-way ANOVA with Sidak post hoc analysis was used for comparisons between groups (GraphPad Prism 9.0, CA, USA). Nonparametric Spearman's rank correlation analysis was used to evaluate the associations between the regional SUVRs of different tracers. $P < 0.05$ indicated statistical significance. The data are presented as the mean ± standard deviation.

Results

Higher Regional [¹⁸F]Florbetapir SUVRs in the Brains of APP/PS1 Mice at 5 and 10 Months of Age

APP/PS1 mice and 3×Tg mice both develop plaque at approximately 6 months of age [34, 59]; however, recent characterization of 3×Tg mice revealed very little pathology at 12 months [35]. Therefore, we chose to investigate the APP/PS1 mice at 5 and 10 months to represent the preplaque and plaque, respectively, and 3×Tg mice at 11 months. We first assessed the distribution of amyloid pathology in these mice using [¹⁸F]florbetapir PET. We used the cerebellum as a reference region for the quantification of the SUVR, as in earlier studies using [¹⁸F]florbetapir imaging in APP/PS1 model [27]. The [¹⁸F]florbetapir SUVR (Cb as the reference region) was greater in the thalamus, basal forebrain system, brainstem, and midbrain of 5-month-old APP/PS1 mice than in age-matched wild-type mice. A greater [¹⁸F]florbetapir SUVR was observed in the cortex and hippocampus of 10-month-old APP/PS1 mice than in age-matched wild-type mice and 5-month-old APP/PS1 mice (Fig. 1). In contrast, no regional differences in [¹⁸F]florbetapir SUVR were observed between the brains of 11-month-old 3×Tg mice and age-matched wild-type mice (Fig. 1e).

To further support our negative [¹⁸F]florbetapir results in the brain of 3×Tg mice, we performed PET using another amyloid tracer, [¹¹C]PIB, in four 3×Tg mice. We used the cerebellum as the reference region for the quantification of [¹¹C]PIB SUVRs in the mouse brain [73]. No difference in the [¹¹C]PIB SUVR was observed in the brains of 11-month-old 3×Tg mice compared to age-matched wild-type mice,

which is in line with our observation by using [¹⁸F]florbetapir (Fig. 1f). No significant between-group differences was observed in [¹⁸F]florbetapir SUVR in the olfactory bulb (SFig. 4a). No significant between-group differences was observed in [¹⁸F]florbetapir SUV in the cerebellum (SFig. 4f).

No Difference in [¹⁸F]PM-PBB3 SUVRs in the Cortex or Hippocampus of APP/PS1 Mice and 3×Tg Mice Compared to WT Mice

The initial study on 3×Tg mice showed that tau deposits developed at 9 months [59]; however, recent characterization suggested that there is a lack of AT-8-positive signals in the hippocampus [35]. In vivo Tau PET has not been reported in 3×Tg mice. We therefore characterized the tau distribution in the brains of APP/PS1 mice at 5 months (as another control group) and 3×Tg mice at 11 months by PET using [¹⁸F]PM-PBB3. [¹⁸F]PM-PBB3 has been used to study tau distribution in tau mouse models [76]. The cerebellum was validated in earlier studies as a reference region for the quantification of the [¹⁸F]PM-PBB3 SUVR [76, 85]. We chose 90 min postinjection for the [¹⁸F]PM-PBB3 static scan based on the time activity curve (SFig. 2) and previous studies [76, 85]. The Cb was used as the reference brain region, as in previous PET studies with [¹⁸F]PM-PBB3 [76]. No regional difference in [¹⁸F]PM-PBB3 SUVR was observed in the brains of 5-month-old APP/PS1 mice or 11-month-old 3×Tg mice compared to age-matched wild-type mice (Fig. 2). No significant between-group differences was observed in [¹⁸F]PM-PBB3 SUVR in the olfactory bulb (SFig. 4b). No significant between-group differences was observed in [¹⁸F]PM-PBB3 SUV in the cerebellum (SFig. 4g).

Increased [¹⁸F]SMBT-1 SUVRs in the Cortex and Hippocampus of 10-month-old APP/PS1 Mice

[¹⁸F]SMBT-1 PET enables the detection of MAO-B, which is upregulated in reactive astrocytes in the human and rodent brain [31]. Here, we evaluated the distribution of [¹⁸F]SMBT-1 and its temporal and spatial relationships with amyloid-beta deposits in the brains of 5- and 10-month-old APP/PS1 mice and 11-month-old 3×Tg mice. First, we performed dynamic scans and evaluated the time-activity curve of [¹⁸F]SMBT-1 in the WT mouse brain. The cerebellum (gray line) showed faster washout and lower uptake at 45 min postinjection than did the other brain regions examined (SFig. 3). We compared cerebellar uptake in all the mouse groups and found no difference in the SUV (SFig. 4). Therefore, we chose 50–60 min after injection of [¹⁸F]SMBT-1 for acquiring the static scans in the following experiment and used the cerebellum as reference region for SUVR calculation.

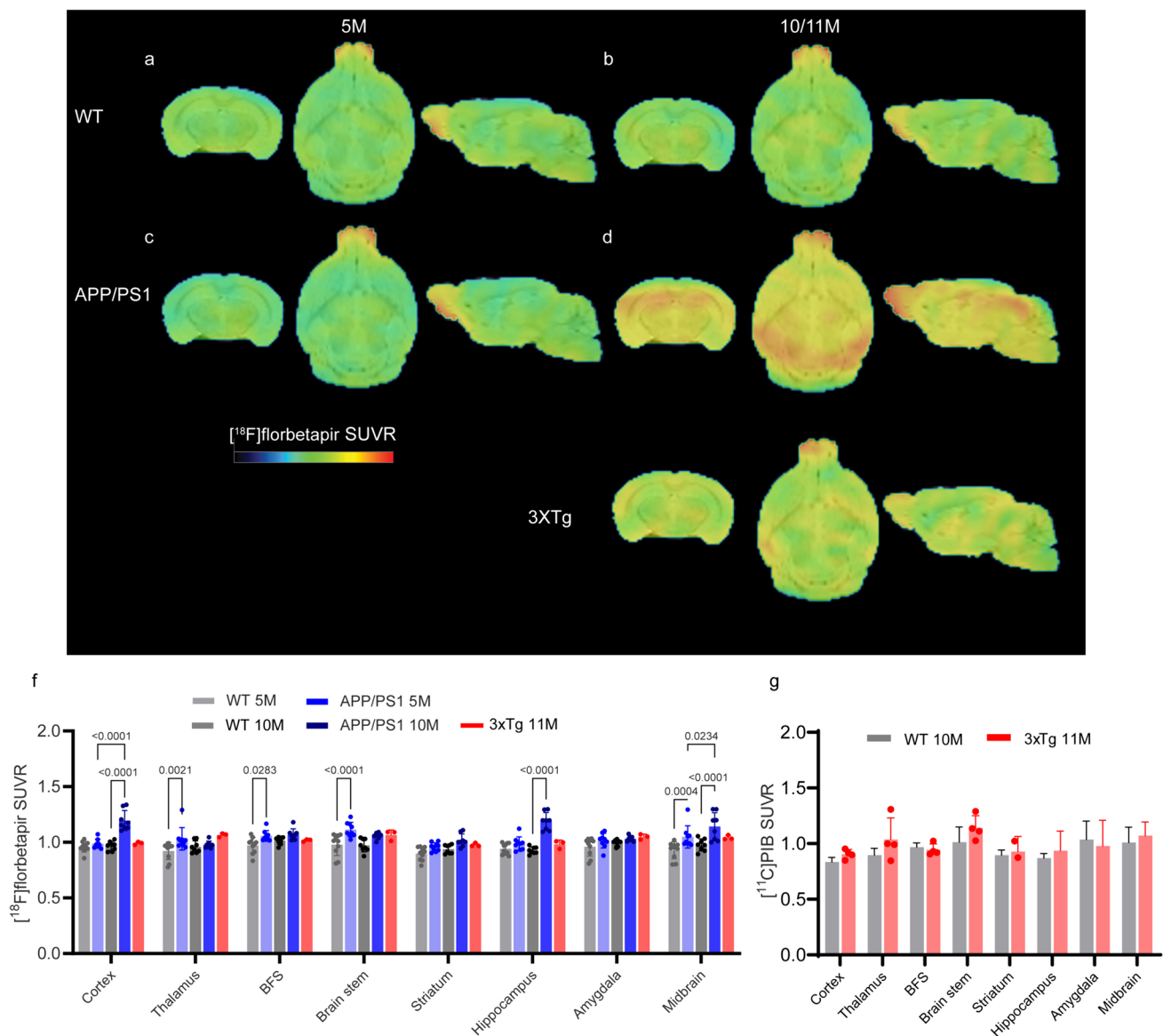


Fig. 1 Increased [^{18}F]florbetapir brain uptake in 10-month-old APP/PS1 mice compared to 5-month-old APP/PS1 mice and age-matched wild-type mice and 3xTg mice. **a–e** Images of SUVRs from 5- and 10-month-old wild-type (WT, **a, b**), 5- and 10-month-old APP/PS1 (**c, d**), and 11-month-old 3xTg mice (**e**). The SUVR scale was 0–2.2.

f Quantification of [^{18}F]florbetapir in WT, APP/PS1, and 3xTg mice using Cb as the reference region. **g** There was no difference in [^{11}C]PIB brain uptake between 3xTg mice and wild-type mice. The SUVR was calculated using the Cb as the reference brain region. BFS, basal forebrain system; BFS, basal forebrain system; Cb, cerebellum

We observed that the [^{18}F]SMBT-1 SUVR (Cb as the reference region) was greater in the cortex and hippocampus of 10-month-old APP/PS1 mice than in 5-month-old APP/PS1 and age-matched wild-type mice. No regional difference in [^{18}F]SMBT-1 SUVR was observed between 11-month-old 3xTg mice and age-matched wild-type mice (Fig. 3a–f). This indicated that the increase in the level of astrocytic MAO-B accompanied amyloid accumulation in the brains of the APP/PS1 mice. [^{18}F]SMBT-1 uptake (SUVR) in the olfactory bulb was rather high in all groups, with no significant between-group differences (SFig. 4c). No significant

between-group differences was observed in [^{18}F]SMBT-1 SUV in the cerebellum (SFig. 4 h).

Glucose Metabolism Comparable Between APP/PS1 Mice and Wild-Type Mice

To assess the changes in cerebral glucose hypometabolism and if there are associations between these changes and other readouts, we performed [^{18}F]FDG imaging in APP/PS1 mice, 3xTg mice and WT mice at 5 and 10–11 months. The cerebellum was chosen as the reference region because

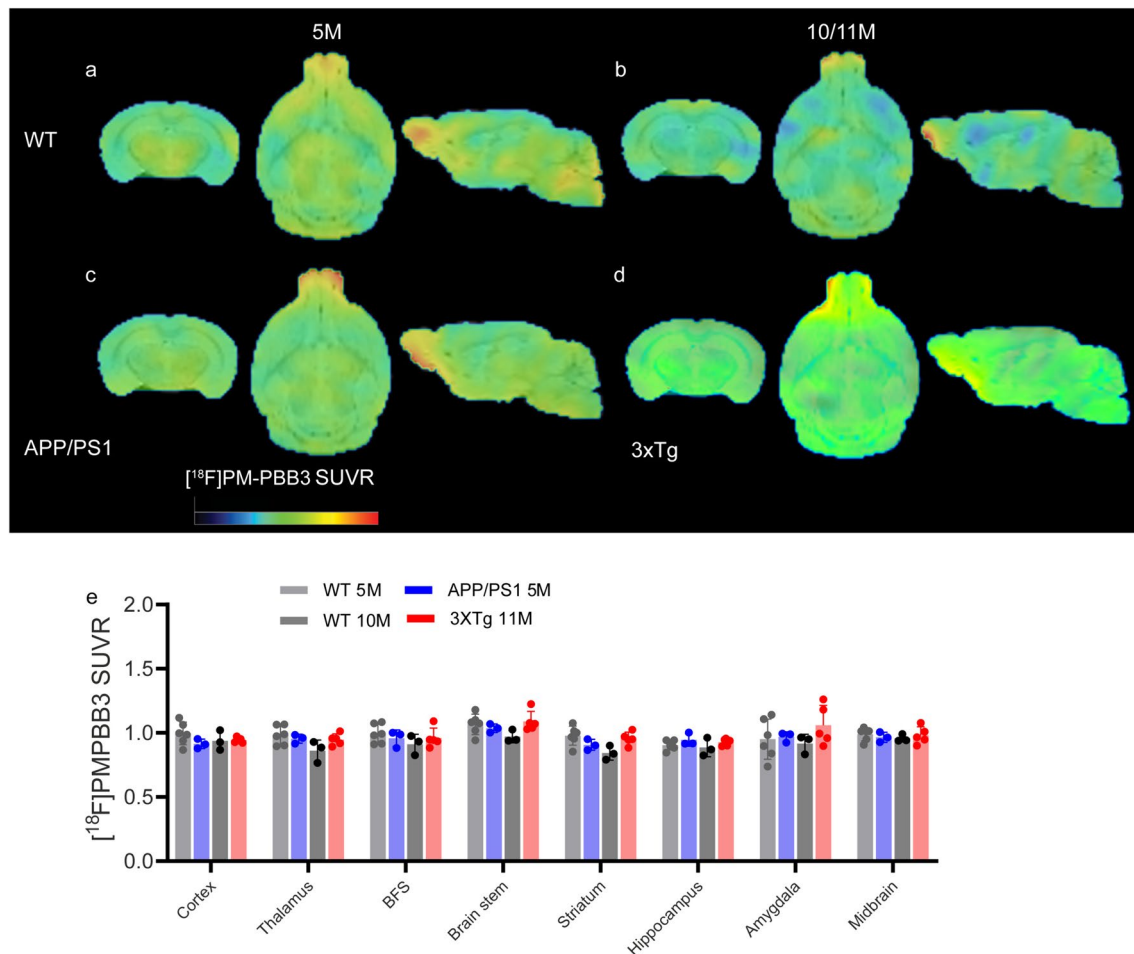


Fig. 2 $[^{18}\text{F}]\text{PM-PBB3}$ brain uptake did not differ between 3xTg mice and age-matched wild-type mice. **a-d** Images of SUVRs from 5- and 10-month-old wild-type (WT, **a, b**), 5-month-old APP/PS1 (**c**), and

11-month-old 3xTg mice (**d**). The SUVR scale was 0–2.2. **e** Quantification of $[^{18}\text{F}]\text{PM-PBB3}$ in WT and 3xTg mice using Cb as the reference brain region. BFS, basal forebrain system; Cb, cerebellum

it was used in earlier studies [74]. The $[^{18}\text{F}]\text{FDG}$ SUVRs (Cb as a reference region) were comparable in different brain regions between 5-month-old and 10-month-old APP/PS1 mice and age-matched wild-type mice (Fig. 4). No regional difference in $[^{18}\text{F}]\text{FDG}$ SUVR was observed in the brains of 11-month-old 3xTg mice compared to age-matched wild-type mice (Fig. 4). No significant between-group differences was observed in $[^{18}\text{F}]\text{FDG}$ SUVR in the olfactory bulb (SFig. 4d). No significant between-group differences were observed in $[^{18}\text{F}]\text{FDG}$ SUV in the cerebellum (SFig. 4i).

$[^{18}\text{F}]\text{DPA-714}$ SUVR Did Not Differ Among APP/PS1 Mice, 3xTg Mice and Wild-Type Mice

PET of TSPO tracers, such as $[^{18}\text{F}]\text{DPA-714}$, has been widely used as an imaging biomarker for indicating microglial activation and neuroinflammation. Next, we assessed the pattern of TSPO by PET using $[^{18}\text{F}]\text{DPA-714}$

in 5- or 10-month-old APP/PS1 mice and 11-month-old 3xTg mice. Different reference brain regions, including the cerebellum [8, 38, 50], hypothalamus [41] and mid-brain [22] (to avoid spillover), have been used for $[^{18}\text{F}]\text{DPA-714}$ SUVR quantification in mouse models. Here, we used the Cb as the reference brain region for $[^{18}\text{F}]\text{DPA-714}$ according to earlier studies using $[^{18}\text{F}]\text{DPA-714}$ and $[^{11}\text{C}]\text{PBR28}$ in mouse models [50], despite the known rather high signal in the cerebellum. No difference in $[^{18}\text{F}]\text{DPA-714}$ SUVR was observed between 5- or 10-month-old APP/PS1 mice and age-matched wild-type mice (Fig. 5). No difference in $[^{18}\text{F}]\text{DPA-714}$ SUVR was observed between 11-month-old 3xTg mice and age-matched wild-type mice (Fig. 5). No significant between-group differences was observed in $[^{18}\text{F}]\text{DPA-714}$ SUVR in the olfactory bulb (SFig. 4e). No significant between-group differences was observed in $[^{18}\text{F}]\text{DPA-714}$ SUV in the cerebellum (SFig. 4j).

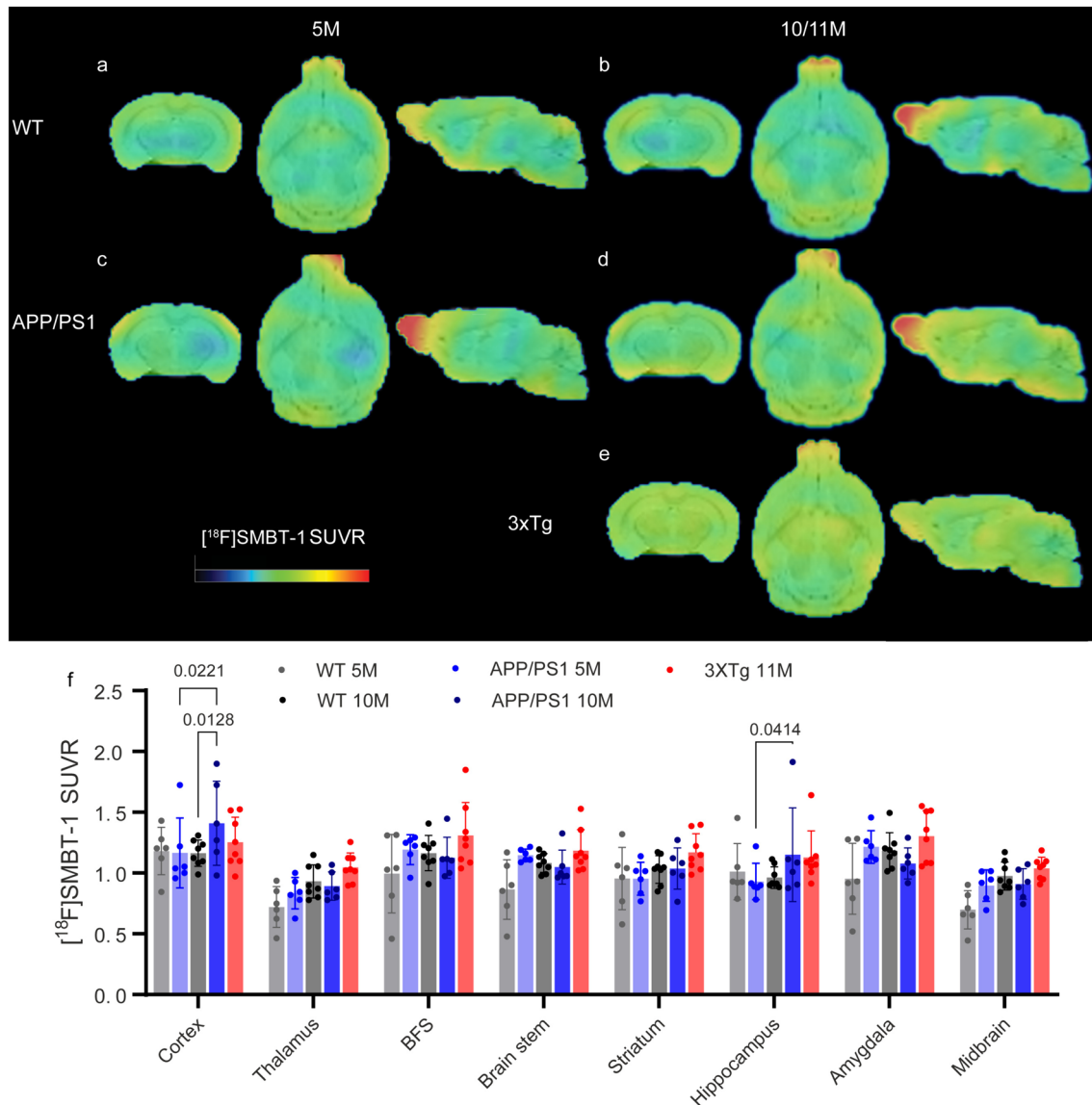


Fig. 3 Increased $[^{18}\text{F}]$ SMBT-1 brain uptake in 10-month-old APP/PS1 mice compared to age-matched wild-type mice. **a–e** Images of SUVRs from 5- and 10-month-old wild-type (WT, **a, b**), 5- and 10-month-old APP/PS1 (**c, d**), and 11-month-old 3xTg mice (**e**).

The SUVR scale was 0–2.2. **f** Quantification of $[^{18}\text{F}]$ SMBT-1 in WT, APP/PS1 and 3xTg mice using Cb as the reference region. BFS, basal forebrain system; Cb, cerebellum

Association Between $[^{18}\text{F}]$ Florbetapir, $[^{18}\text{F}]$ PM-PBB3, $[^{18}\text{F}]$ SMBT-1, $[^{18}\text{F}]$ FDG, and $[^{18}\text{F}]$ DPA-714

To assess the spatial association between different pathologies, nonparametric Spearman's rank correlation analysis was performed on the regional SUVR readouts for $[^{18}\text{F}]$ SMBT-1, $[^{18}\text{F}]$ florbetapir $[^{18}\text{F}]$ PM-PBB3, $[^{18}\text{F}]$ FDG, and $[^{18}\text{F}]$ DPA-714 within the transgenic group. Although the $[^{18}\text{F}]$ DPA-714 level was not significantly different between the transgenic and WT groups, positive correlations were

observed between $[^{18}\text{F}]$ florbetapir SUVR and $[^{18}\text{F}]$ DPA-714 SUVR in the cortex ($r=0.6214$, $p=0.0155$, $n=15$) and in the hippocampus ($r=0.7071$, $p=0.0042$, $n=15$) among the transgenic mice (both APP/PS1 and 3xTg mice; Fig. 5g, h). Positive correlations were observed between the $[^{18}\text{F}]$ florbetapir SUVR and $[^{18}\text{F}]$ DPA-714 SUVR in the cortex ($r=0.6014$, $p=0.0428$; $n=12$) and in the hippocampus ($r=0.7273$, $p=0.0096$, $n=12$) within the APP/PS1 mice. No other regional correlation was found between different readouts.

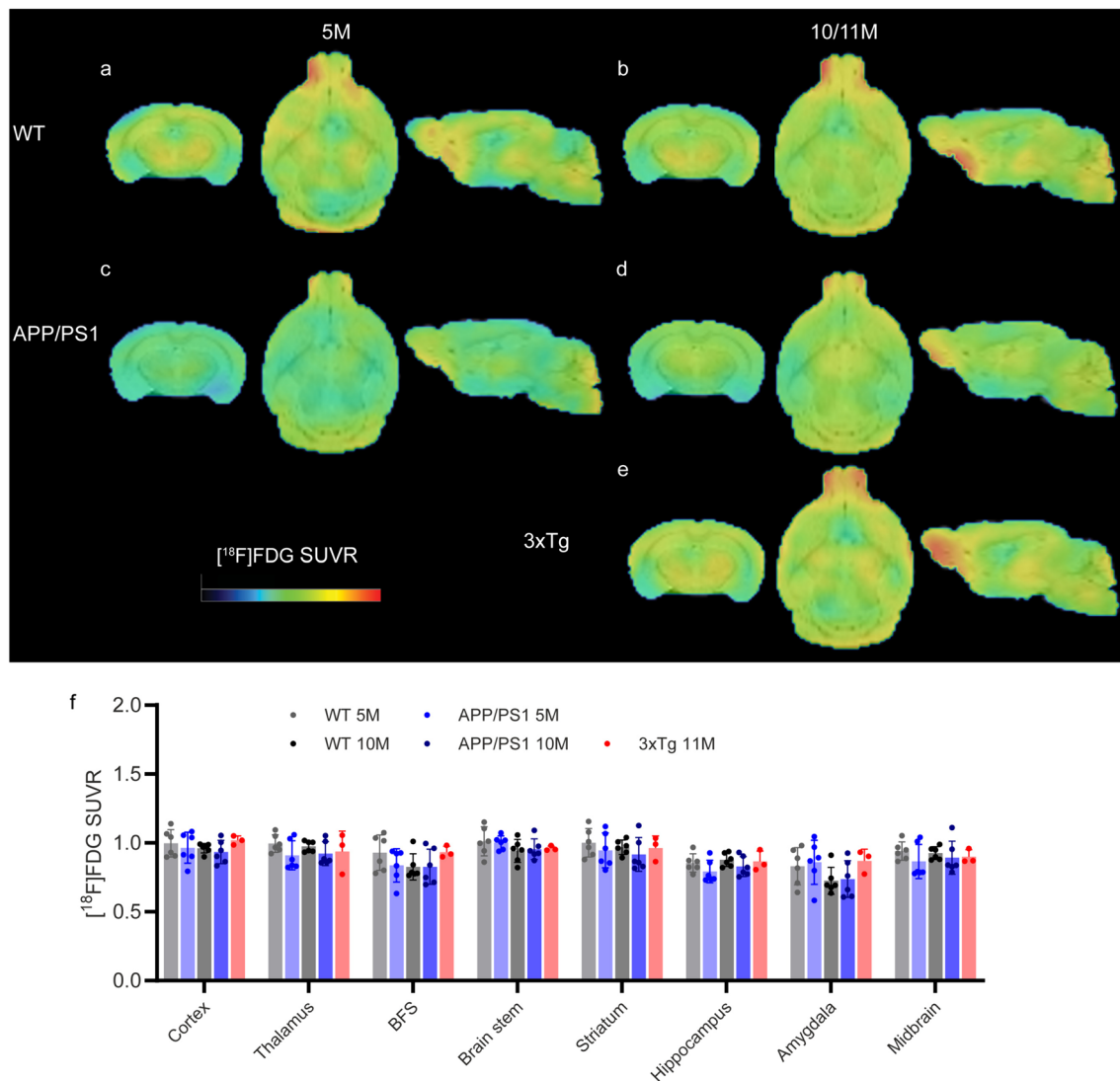


Fig. 4 $[^{18}\text{F}]\text{FDG}$ brain uptake was lower in 5-month-old APP/PS1 mice than in age-matched wild-type mice. **a–e** Images of SUVRs from 5- and 10-month-old wild-type (WT, **a, b**), 5- and 10-month-old APP/PS1 (**c, d**), and 11-month-old 3xTg mice (**e**). The SUVR scale

was 0–1.8. **f** Quantification of $[^{18}\text{F}]\text{FDG}$ using Cb as the reference brain region in WT, APP/PS1, and 3xTg mice. BFS, basal forebrain system; Cb, cerebellum

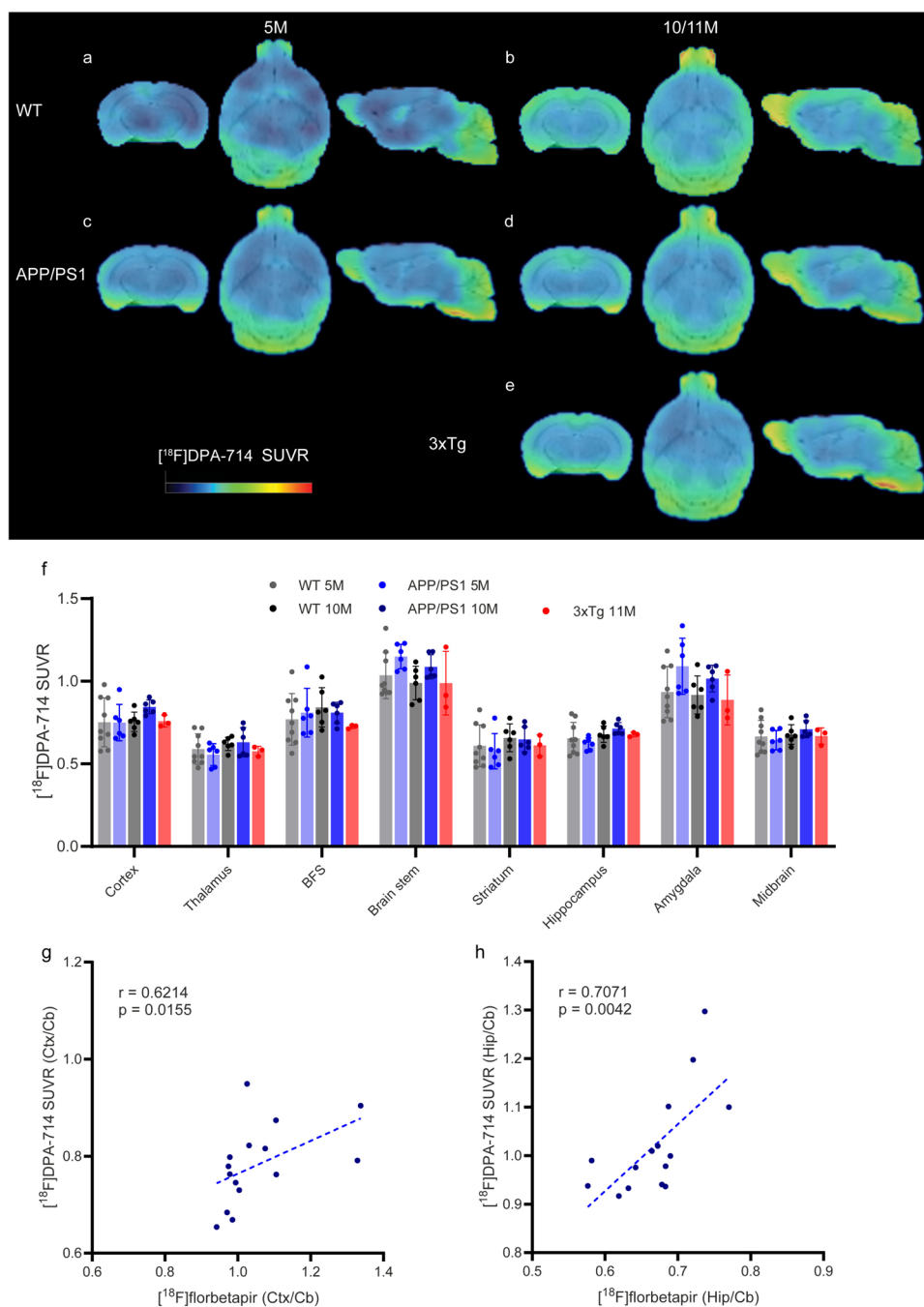
Reactive Astrocytes and Microgliosis with Tau Inclusions and A β Deposits

Next, we evaluated the distributions of MAO-B and TSPO along with the astrocytic markers GFAP/C3d and A β deposits (6E10) and GluT1 in brain tissue slices. Given the age of the mice, autofluorescence of the brain tissue was assessed (SFig. 5). Only autofluorescence affects the DAPI channel due to the presence of amyloid-beta plaques (a representative image shows the subiculum of a 3xTg mouse). MAO-B was detected on astrocytes via colocalization with C3D immunofluorescence in the cortex and hippocampus of APP/PS1 and 3xTg mice and was found to colocalize with A1 reactive astrocytes (Fig. 6b, c). The

MAO-B distribution appears to be greater in the white matter than in the gray matter of the mouse brain. The MAO-B signal in the cerebellum was low, indicating that the cerebellum is suitable as a reference brain region.

In 3xTg mice at 11 months, limited A β deposits (mainly intracellular) and tau inclusions were observed, mainly in the subiculum and CA1 region of the hippocampus (Fig. 7a–c, e, f), validating the lack of amyloid PET ($[^{18}\text{F}]\text{florbetapir}$, $[^{11}\text{C}]\text{PIB}$) and tau PET ($[^{18}\text{F}]\text{PM-PBB3}$) updates in the mouse brain. This finding is different from the abundant amyloid deposits in the cortex, hippocampus and thalamus of APP/PS1 mice at 10 months (Fig. 7d). Similarly, the levels of the glucose transport protein GluT1 were detected in the cortex and hippocampus of 3xTg mice and wild-type mice (SFig. 6).

Fig. 5 Comparable [^{18}F]DPA-714 brain uptake in 5-month- and 10-month-old APP/PS1 mice, age-matched wild-type mice and 3 \times Tg mice. **a–e** Images of SUVRs from 5- and 10-month-old wild-type (WT, **a, b**), 5- and 10-month-old APP/PS1 (**c, d**), and 11-month-old 3 \times Tg mice (**e**). The SUVR scale was 0–2.2. **f** Quantification of the regional [^{18}F]DPA-714 SUVR using Cb as the reference brain region in WT, APP/PS1 and 3 \times Tg mice. **g, h** Correlations between [^{18}F]florbetapir SUVR and [^{18}F]DPA-714 SUVR in the cortex (Ctx) and hippocampus (Hip) of mouse brains were assessed using Cb as the reference brain region. BFS, basal forebrain system; Cb, cerebellum



Discussion

Here, we demonstrated increased brain regional [^{18}F]SMBT-1 and [^{18}F]florbetapir brain uptake in 10-month-old APP/PS1 mice and comparable [^{18}F]FDG and [^{18}F]DPA-714 uptake compared to age-matched wild-type mice. Moreover, [^{18}F]DPA-714 uptake correlated with [^{18}F]florbetapir in the cortex and hippocampus, whereas no correlation was found between the uptake of [^{18}F]SMBT-1 and other tracers in the brain.

For amyloid imaging, several microPET studies using [^{18}F]florbetapir [7, 20, 64, 84], [^{18}F]florbetaben, [^{11}C]PIB [54, 55], and [^{18}F]flutemetamol in APP/PS1 mice have been reported. Our finding of increased [^{18}F]florbetapir SUVRs in the cortex and hippocampus was in line with the known A β aggregate distribution and immunofluorescence staining in the brains of APP/PS1 mice. Our observation of a lack of increase in [^{18}F]florbetapir uptake in 3 \times Tg mice is in line with previous observations using [^{11}C]PIB (or [^{18}F]florbetaben) [62] in 3 \times Tg mice at 4–16 months [15, 16] but

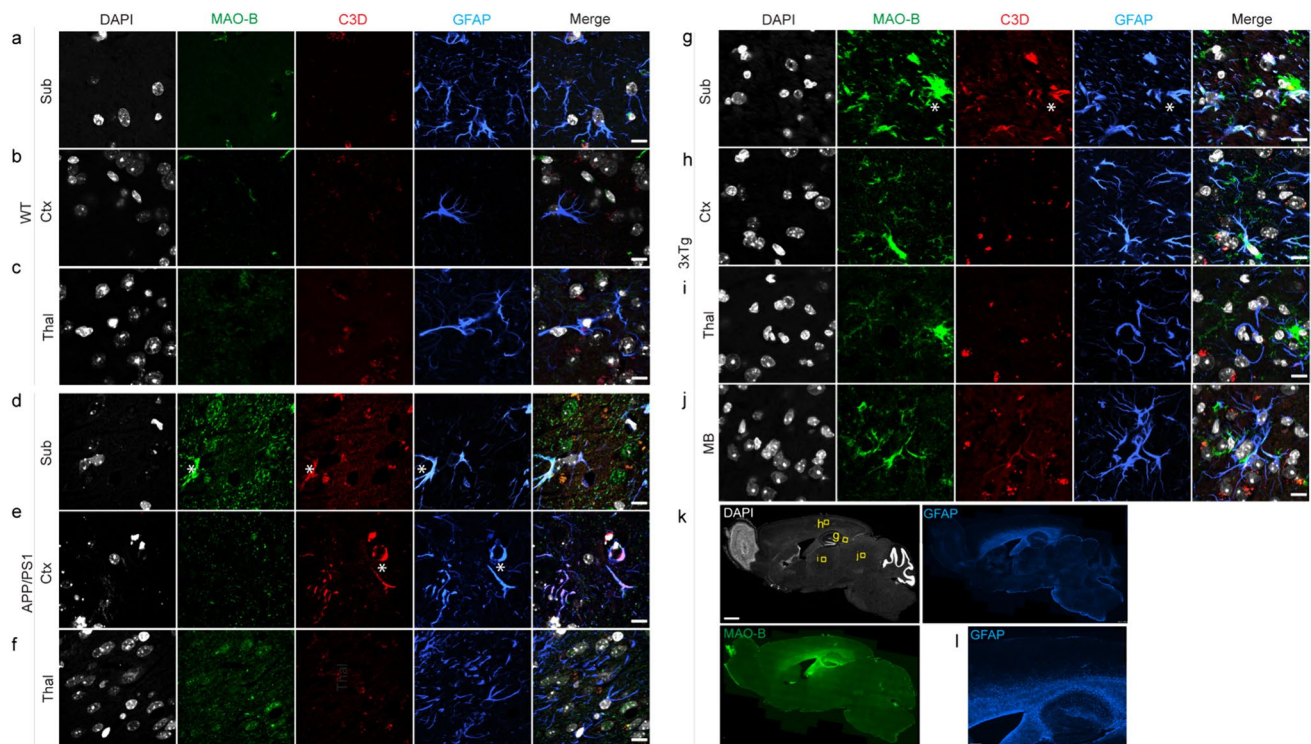


Fig. 6 Immunofluorescence staining of MAO-B and astrocyte markers in mouse brains. Brain tissue sections from wild-type (WT), APP/PS1 and 3×Tg mice were stained for MAO-B (green)/C3D (red)/GFAP (blue). **a–j** Zoomed-in view showing the colocalization of MAO-B on C3D-positive astrocytes in the subiculum (Sub), cor-

tex (Ctx), thalamus (Thal), and midbrain (MB). **k–l** Overview of the staining in 3×Tg mice showing the location of the regions (**g**, **h**, **i**, **j**). Nuclei were counterstained with DAPI (gray). * indicates colocalization. Scale bar = 10 μm (**a–j**), 1 mm (**k**), and 200 μm (**l**)

differs from two other studies showing an increase at 8 and 10 months [15, 78]. We also found a limited distribution of Aβ (6E10) immunoreactivity in the brains of 11-month-old 3×Tg mice (few in the subiculum). Although high loads of amyloid and tau were observed in the original study [59], a recent study in 3×Tg mice from LaFerla lab showed that there is a lack of Thioflavin-S-positive amyloid staining in the brains of 12-month-old 3×Tg mice, likely due to genetic drift [35]. For tau imaging, PET has been performed using [¹¹C]PBB3, [¹⁸F]PM-PBB3, and [¹⁸F]PI-2620 in PS19 and rTg4510 mice [4, 9, 22, 33, 42, 56, 61], as well as [¹¹C]THK5317 [25] and [¹¹C]THK5117 [12], which bind to both tau and MAO-B, in double mutant TgF344 rats. Thus far, only one ex vivo [¹⁸F]flortaucipir autoradiography study of aged APP/PS1 mouse brain slices with positive result [52]. We observed no change in the [¹⁸F]PM-PBB3 SUVR in the APP/PS1 mice at 5 months or in 3×Tg mice. Our AT-8 immunofluorescence staining showed that the tau inclusions in the brain of 3×Tg mice was rather limited. Many reports have shown that 3×Tg mice exhibit significant neurofibrillary tangles in the brain at this age [18, 59]; however, a recent study in 3×Tg mice from the LaFerla lab showed that there is a lack of phospho-Tau (AT-8) positive staining but high HT-7-positive total tau immunoreactivity in the

hippocampus of 3×Tg mice at 12 months [35]. Therefore, the difference in the tau load might be due to genetic drift and the choice of antibody.

We found increased cortical and hippocampal MAO-B levels in 10-month-old APP/PS1 mice compared to wild-type mice but no difference in 11-month-old 3×Tg mice according to [¹⁸F]SMBT-1 PET. No earlier study has reported MAO-B imaging results in APP/PS1 mice. Nevertheless, an early increase in MAO-B has been reported in the thalamus of PS2APP mice at 5, 13, and 19 months and in the hippocampus at 14 and 19 months compared with that in wild-type mice by using [¹⁸F]F-DED [3], and in 6-month-old APPswe mice preceding amyloid plaque deposition using [¹¹C]AZD2184 [66] using [¹¹C]DED. Our lack of difference in [¹⁸F]SMBT-1 uptake in 3×Tg mice is in line with the findings of a recent study in which [¹¹C]DED was used to evaluate the hippocampus or cortex of 10-month-old 3×Tg mice. However, another study using [¹⁸F]sulforhodamine-101 showed that uptake increased in 9- to 10-month-old 3×Tg mice [45]. Notably, [¹⁸F]Sulforhodamine-101 detects the thyroid hormone transporter OATP1C1, which is located mainly on astrocytes and endothelial cells, unlike [¹⁸F]SMBT-1, which targets MAO-B located on astrocytes and neurons.

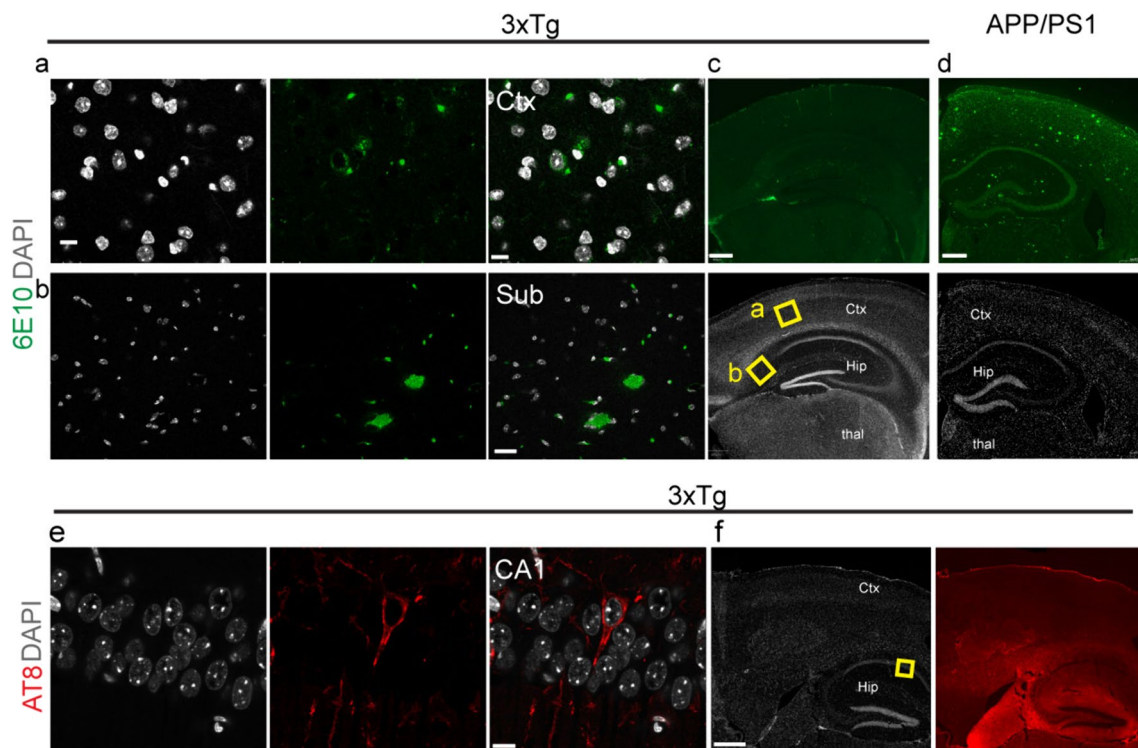


Fig. 7 Limited amyloid-beta deposits and tau inclusions in the brains of 3×Tg mice and amyloid-beta plaques. **a–c** Limited amyloid deposits were observed in the subiculum and cortex (layer 3/4) brain tissue sections of 11-month-old 3×Tg mice stained for 6E10 (mainly intracellular); yellow squares in **c** indicate the locations of the zoomed-in view (**a**, **b**). **d** Amyloid deposits were abundant in the cortex (Ctx) and hippocampus (Hip) and in the thalamus (Thal) of 10-month-old

APP/PS1 mice. **e**, **f** Limited tau inclusion was observed in the hippocampus (CA1) of 3×Tg mice stained for AT-8. The yellow squares in **f** indicate the locations enlarged in view (**e**). The anti-amyloid antibody 6E10 (green) and the anti-phospho-Tau antibody AT-8 (red) were used. Nuclei were counterstained with DAPI (white). Scale bars = 10 mm (**a**, **b**, **e**) and 400 μm (**c**, **d**, **f**)

Inconsistent results have been reported for [^{18}F]FDG updates in animal models of AD, partly due to differences in the imaging protocol, fasting, anesthesia depth, sex, age, and heterogeneity between animals. Here, we found no difference in [^{18}F]FDG uptake between 5- or 10-month-old APP/PS1 mice or between 11-month-old 3×Tg mice and wild-type mice. Higher [^{18}F]FDG uptake in the brain of increase in 2, 3, 5, and 8 months old APP/PS1 mice [47] as well as 12-month-old APP/PS1 mice [65, 74] has been reported. While several other studies found that [^{18}F]FDG uptake was lower in the brain of 6-month-old [68] and 11-month-old 3×Tg mice [1] than in WT mice; In addition, one study showed that there was no difference in [^{18}F]FDG uptake detected in the brain of 12 months 3×Tg mice [58] compared to WT mice.

TSPO is overexpressed on activated macrophages and microglia and is considered a biomarker of neuroinflammation [46]. TSPO tracers [46, 87], including 1st generation [^{11}C]PK11195, 2nd generation [^{18}F]DPA-714, [^{11}C]PBR28, and 3rd generation [^{18}F]GE-180, have been the most widely used. Notably, the increase in the TSPO PET signal does not necessarily indicate microglial proliferation. [^{18}F]

DPA-714 showed favorable binding potential and selectivity and low nonspecific binding compared to [^{11}C]PK11195 [14]. We observed no difference in the brain regional [^{18}F]DPA-714 SUVR (Cb as reference region) between 5- or 10-month-old APP/PS1 mice and wild-type mice. However, a positive correlation was observed between [^{18}F]DPA-714 and [^{18}F]florbetapir SUVR in the cortex and between [^{18}F]DPA-714 and hippocampus in APP/PS1 mice and in APP/PS1 combined with 3×Tg mice. These findings indicate a close link between microgliosis and amyloid deposition. Several imaging studies have reported an increase in TSPO levels in APP/PS1 mice; [^{11}C]PK11195 uptake increased at 16–19 months APP/PS1 mice (not at 13–16 months) compared to WT mice [79]; [^{18}F]GE180 uptake increased at 26 months APP/PS1 mice compared to 4 months APP/PS1 mice [48]; [^{18}F]DPA-714 uptake increased at 12 months [75] and at 18 months APP/PS1 mice compared to WT mice [11]. For 3×Tg mice, one study of [^{11}C]PK11195 showed that the level was comparable to control at 4–16 months [16], while another study revealed an increase in the hippocampus at 10 months compared to wild-type mice using [^{125}I]CLINDE [78].

This study has several limitations. First, the mice were cross-sectional, not longitudinal. Only 3×Tg mice of one age were chosen. The sample size of the 3×Tg mouse group and the sex balance of the animals were not optimal. Different 3×Tg mice were used for in vivo imaging and ex vivo staining. Moreover, we did not provide detailed information on the morphology or heterogeneity of astrocytes and microglia or whether the astrocytes were vessel associated or associated with pathology. Notably, there are distinct dynamic profiles of microglial activation [30] and reactive astrocytes between human and mouse models [19].

Conclusion

Here, we showed increased levels of [¹⁸F]SMBT-1 and [¹⁸F]florbetapir in the brains of 10-month-old APP/PS1 mice compared to age-matched wild-type mice, preceding changes in the level of [¹⁸F]DPA-714. The [¹⁸F]florbetapir and [¹⁸F]DPA-714 SUVRs correlated in the hippocampus and cortex of the transgenic mice.

Supplementary Information The online version contains supplementary material available at <https://doi.org/10.1007/s12035-024-04106-7>.

Acknowledgements The authors acknowledge the Center for Microscopy and Image Analysis (ZMB), Mr Miles Gisler, ETH Zurich and Mr. Daniel Schuppli, IREM, University of Zurich.

Author Contribution The study was designed by YK and RN. YK performed the radiosynthesis, HPLC, and microPET analyses. CM performed the staining and microscopy. RN performed the microPET analysis. YK, CM, and RN wrote the first draft. All the authors contributed to the revision of the manuscript. All the authors have read and approved the final manuscript.

Funding Open access funding provided by University of Zurich. YK received funding from the National Natural Science Foundation of China (No. 82272108, 81701732), the Natural Science Foundation of Shanghai (No. 22ZR1409200), and the Shanghai Science and Technology Innovation Action Plan Medical Innovation Research Project (23Y11903200). YG received funding from the NSFC (82071962). RN acknowledged support from the Swiss Center for Advanced Human Toxicity (SCAHT-AP_22_02), the EU Joint Programme – Neurodegenerative Disease Research grant JPND2022-083, the Innosuisse – Swiss Innovation Agency grant 51767.1 IP-LS. Zurich Neuroscience Zentrum and Helmut Horten Stiftung.

Data Availability The datasets generated and/or analyzed during the current study are available from the corresponding author upon reasonable request.

Declarations

Ethics Approval The PET imaging and experimental protocol were approved by the Institutional Animal Care and Ethics Committee of Fudan University and performed in accordance with the National Research Council's Guide for the Care and Use of Laboratory Animals. All the experiments in Zurich were performed in accordance with the

Swiss Federal Act on Animal Protection and were approved by the Cantonal Veterinary Office Zurich (ZH162/20).

Consent to Participate Not applicable.

Consent for Publication Not applicable.

Competing Interests RMN is employee and shareholder of Neurimmune AG, Switzerland.

The other authors declare no competing interests.

Open Access This article is licensed under a Creative Commons Attribution 4.0 International License, which permits use, sharing, adaptation, distribution and reproduction in any medium or format, as long as you give appropriate credit to the original author(s) and the source, provide a link to the Creative Commons licence, and indicate if changes were made. The images or other third party material in this article are included in the article's Creative Commons licence, unless indicated otherwise in a credit line to the material. If material is not included in the article's Creative Commons licence and your intended use is not permitted by statutory regulation or exceeds the permitted use, you will need to obtain permission directly from the copyright holder. To view a copy of this licence, visit <http://creativecommons.org/licenses/by/4.0/>.

References

- Adlimoghaddam A, Snow WM, Stortz G, Perez C, Djordjevic J, Goertzen AL, Ko JH, Albensi BC (2019) Regional hypometabolism in the 3xTg mouse model of Alzheimer's disease. *Neurobiol Dis* 127:264–277
- Andersen JV, Skotte NH, Christensen SK, Polli FS, Shabani M, Markussen KH, Haukedal H, Westi EW et al (2021) Hippocampal disruptions of synaptic and astrocyte metabolism are primary events of early amyloid pathology in the 5xFAD mouse model of Alzheimer's disease. *Cell Death Dis* 12(11):954
- Ballweg A, Klaus C, Vogler L, Katzdobler S, Wind K, Zatcepin A, Ziegler SI, Secgin B et al (2023) [¹⁸F]F-DPA PET imaging of reactive astrogliosis in neurodegenerative diseases: preclinical proof of concept and first-in-human data. *J Neuroinflammation* 20(1):68
- Barron AM, Ji B, Fujinaga M, Zhang MR, Suhara T, Sahara N, Aoki I, Tsukada H et al (2020) In vivo positron emission tomography imaging of mitochondrial abnormalities in a mouse model of tauopathy. *Neurobiol Aging* 94:140–148
- Bellaver B, Povala G, Ferreira PCL, Ferrari-Souza JP, Leffa DT, Lussier FZ, Benedet AL, Ashton NJ et al (2023) Astrocyte reactivity influences amyloid-β effects on tau pathology in preclinical Alzheimer's disease. *Nat Med* 29(7):1775–1781
- Beyer L, Stocker H, Rujescu D, Hollecsek B, Stockmann J, Nabers A, Brenner H, Gerwert K (2023) Amyloid-beta misfolding and GFAP predict risk of clinical Alzheimer's disease diagnosis within 17 years. *Alzheimers Dement* 19:1020–1028
- Biechele G, Sebastian Monasor L, Wind K, Blume T, Parhizkar S, Arzberger T, Sacher C, Beyer L et al (2022) Glitter in the darkness? Non-fibrillar β-amyloid plaque components significantly impact the β-amyloid PET signal in mouse models of Alzheimer's Disease. *J Nucl Med* 63(1):117–124
- Brendel M, Probst F, Jaworska A, Overhoff F, Korzhova V, Albert NL, Beck R, Lindner S et al (2016) Glial activation and glucose metabolism in a transgenic amyloid mouse model: a triple-tracer PET study. *J Nucl Med* 57(6):954–960

9. Cao L, Kong Y, Ji B, Ren Y, Guan Y, Ni R (2021) Positron emission tomography in animal models of tauopathies. *Front Aging Neurosci* 13:761913
10. Carter SF, Schöll M, Almkvist O, Wall A, Engler H, Långström B, Nordberg A (2012) Evidence for astrogliosis in prodromal Alzheimer disease provided by 11C-deuterium-L-deprenyl: a multitracers PET paradigm combining 11C-Pittsburgh compound B and 18F-FDG. *J Nucl Med* 53(1):37–46
11. Chaney A, Bauer M, Bochicchio D, Smigova A, Kassiou M, Davies KE, Williams SR, Boutin H (2018) Longitudinal investigation of neuroinflammation and metabolite profiles in the APP(swe) xPS1(Δe9) transgenic mouse model of Alzheimer's disease. *J Neurochem* 144(3):318–335
12. Chaney AM, Lopez-Picon FR, Serrière S, Wang R, Bochicchio D, Webb SD, Vandesquille M, Harte MK et al (2021) Prodromal neuroinflammatory, cholinergic and metabolite dysfunction detected by PET and MRS in the TgF344-AD transgenic rat model of AD: a collaborative multi-modal study. *Theranostics* 11(14):6644–6667
13. Chatterjee P, Pedrini S, Stoops E, Goozee K, Villemagne VL, Asih PR, Verberk IMW, Dave P et al (2021) Plasma glial fibrillary acidic protein is elevated in cognitively normal older adults at risk of Alzheimer's disease. *Transl Psychiatry* 11(1):27
14. Chauveau F, Van Camp N, Dollé F, Kuhnast B, Hinnen F, Damont A, Boutin H, James M et al (2009) Comparative evaluation of the translocator protein radioligands 11C-DPA-713, 18F-DPA-714, and 11C-PK11195 in a rat model of acute neuroinflammation. *J Nucl Med* 50(3):468–476
15. Chen YA, Lu CH, Ke CC, Chiu SJ, Chang CW, Yang BH, Gelovani JG, Liu RS (2021) Evaluation of class IIa histone deacetylases expression and in vivo epigenetic imaging in a transgenic mouse model of Alzheimer's disease. *Int J Mol Sci* 22(16):8633
16. Chiquita S, Ribeiro M, Castelhana J, Oliveira F, Sereno J, Batista M, Abrunhosa A, Rodrigues-Neves AC et al (2019) A longitudinal multimodal in vivo molecular imaging study of the 3xTg-AD mouse model shows progressive early hippocampal and taurine loss. *Hum Mol Genet* 28(13):2174–2188
17. Chun H, Im H, Kang YJ, Kim Y, Shin JH, Won W, Lim J, Ju Y et al (2020) Severe reactive astrocytes precipitate pathological hallmarks of Alzheimer's disease via H(2)O(2)(-) production. *Nat Neurosci* 23(12):1555–1566
18. Dai C-I, Hu W, Tung YC, Liu F, Gong C-X, Iqbal K (2018) Tau passive immunization blocks seeding and spread of Alzheimer hyperphosphorylated Tau-induced pathology in 3 x Tg-AD mice. *Alzheimer's Res Ther* 10(1):13
19. De Bastiani MA, Bellaver B, Brum WS, Souza DG, Ferreira PCL, Rocha AS, Povala G, Ferrari-Souza JP et al (2023) Hippocampal GFAP-positive astrocyte responses to amyloid and tau pathologies. *Brain Behav Immun* 110:175–184
20. Deleze S, Waldron AM, Verhaeghe J, Bottelbergs A, Wyffels L, Van Broeck B, Langlois X, Schmidt M et al (2017) Evaluation of small-animal PET outcome measures to detect disease modification induced by BACE inhibition in a transgenic mouse model of Alzheimer disease. *J Nucl Med* 58(12):1977–1983
21. Drake LR, Brooks AF, Mufarreh AJ, Pham JM, Koeppe RA, Shao X, Scott PJH, Kilbourn MR (2018) Deuterium Kinetic Isotope Effect Studies of a Potential in Vivo Metabolic Trapping Agent for Monoamine Oxidase B. *ACS Chem Neurosci* 9(12):3024–3027
22. Endepols H, Anglada-Huguet M, Mandelkow E, Schmidt Y, Krapf P, Zlatopolskiy BD, Neumaier B, Mandelkow E-M et al (2022) Assessment of the in vivo relationship between cerebral hypometabolism, tau deposition, TSPO Expression, and synaptic density in a tauopathy mouse model: a multi-tracer PET study. *Mol Neurobiol* 59(6):3402–3413
23. Escartin C, Galea E, Lakatos A, O'Callaghan JP, Petzold GC, Serrano-Pozo A, Steinhäuser C, Volterra A et al (2021) Reactive astrocyte nomenclature, definitions, and future directions. *Nat Neurosci* 24(3):312–325
24. Ferrari-Souza JP, Ferreira PCL, Bellaver B, Tissot C, Wang YT, Lefla DT, Brum WS, Benedet AL et al (2022) Astrocyte biomarker signatures of amyloid-β and tau pathologies in Alzheimer's disease. *Mol Psychiatry* 27(11):4781–4789
25. Filip T, Mairinger S, Neddens J, Sauberer M, Flunkert S, Stanek J, Wanek T, Okamura N et al (2021) Characterization of an APP/tau rat model of Alzheimer's disease by positron emission tomography and immunofluorescent labeling. *Alzheimer's Res Ther* 13(1):175
26. Fontana IC, Kumar A, Okamura N, Nordberg A (2024) Multi-tracer approach to understanding the complexity of reactive astrogliosis in Alzheimer's brains. *ACS Chem Neurosci* 15(2):328–336
27. Frost GR, Longo V, Li T, Jonas LA, Judenhofer M, Cherry S, Koutcher J, Lekay C et al (2020) Hybrid PET/MRI enables high-spatial resolution, quantitative imaging of amyloid plaques in an Alzheimer's disease mouse model. *Sci Rep* 10(1):10379
28. Galea E, Morrison W, Hudry E, Arbel-Ornath M, Bacskai BJ, Gómez-Isla T, Stanley HE, Hyman BT (2015) Topological analyses in APP/PS1 mice reveal that astrocytes do not migrate to amyloid-β plaques. *Proc Natl Acad Sci U S A* 112(51):15556–15561
29. Gulyás B, Pavlova E, Kása P, Gulya K, Bakota L, Várszegi S, Keller E, Horváth MC et al (2011) Activated MAO-B in the brain of Alzheimer patients, demonstrated by [11C]-L-deprenyl using whole hemisphere autoradiography. *Neurochem Int* 58(1):60–68
30. Hamelin L, Lagarde J, Dorothée G, Potier MC, Corlier F, Kuhnast B, Caillé F, Dubois B et al (2018) Distinct dynamic profiles of microglial activation are associated with progression of Alzheimer's disease. *Brain* 141(6):1855–1870
31. Harada R, Hayakawa Y, Ezura M, Lerdsiriruk P, Du Y, Ishikawa Y, Iwata R, Shidahara M et al (2021) (18)F-SMBT-1: a selective and reversible PET tracer for monoamine oxidase-B imaging. *J Nucl Med* 62(2):253–258
32. Hu W, Pan D, Wang Y, Bao W, Zuo C, Guan Y, Hua F, Yang M et al (2020) PET imaging for dynamically monitoring neuroinflammation in APP/PS1 mouse model using [(18)F]DPA714. *Front Neurosci* 14:810
33. Ishikawa A, Tokunaga M, Maeda J, Minamihisamatsu T, Shimojo M, Takuwa H, Ono M, Ni R et al (2018) In vivo visualization of tau accumulation, microglial activation, and brain atrophy in a mouse model of tauopathy rTg4510. *J Alzheimers Dis* 61(3):1037–1052
34. Jankowsky JL, Fadale DJ, Anderson J, Xu GM, Gonzales V, Jenkins NA, Copeland NG, Lee MK et al (2004) Mutant presenilins specifically elevate the levels of the 42 residue beta-amyloid peptide in vivo: evidence for augmentation of a 42-specific gamma secretase. *Hum Mol Genet* 13(2):159–170
35. Javonillo DI, Tran KM, Phan J, Hingco E, Kramár EA, da Cunha C, Forner S, Kawauchi S et al (2021) Systematic phenotyping and characterization of the 3xTg-AD mouse model of Alzheimer's disease. *Front Neurosci* 15:785276
36. Jiwaji Z, Tiwari SS, Avilés-Reyes RX, Hooley M, Hampton D, Torvell M, Johnson DA, McQueen J et al (2022) Reactive astrocytes acquire neuroprotective as well as deleterious signatures in response to Tau and Aβ pathology. *Nat Commun* 13(1):135
37. Jo S, Yarishkin O, Hwang YJ, Chun YE, Park M, Woo DH, Bae JY, Kim T et al (2014) GABA from reactive astrocytes impairs memory in mouse models of Alzheimer's disease. *Nat Med* 20(8):886–896
38. Kang S, Kim J, Lee SY, Okamura N, Chang KA (2022) MicroPET imaging assessment of brain tau and amyloid deposition in 6 x Tg Alzheimer's disease model mice. *Int J Mol Sci* 23(10):5485

39. Kawamura K, Hashimoto H, Furutsuka K, Ohkubo T, Fujishiro T, Togashi T, Arashi D, Sakai T et al (2021) Radiosynthesis and quality control testing of the tau imaging positron emission tomography tracer [(18)F]JPM-PBB3 for clinical applications. *J Labelled Comp Radiopharm* 64(3):109–119
40. Kecheliev V, Boss L, Maheshwari U, Konietzko U, Keller A, Razansky D, Nitsch RM, Klohs J et al (2023) Aquaporin 4 is differentially increased and dislocated in association with tau and amyloid-beta. *Life Sci* 321:121593
41. Keller T, López-Picón FR, Krzyczmonik A, Forsback S, Kirjavainen AK, Takkinen JS, Alzghool O, Rajander J et al (2018) [18F]F-DPA for the detection of activated microglia in a mouse model of Alzheimer's disease. *Nucl Med Biol* 67:1–9
42. Kimura T, Ono M, Seki C, Sampei K, Shimojo M, Kawamura K, Zhang MR, Sahara N et al (2022) A quantitative in vivo imaging platform for tracking pathological tau depositions and resultant neuronal death in a mouse model. *Eur J Nucl Med Mol Imaging* 49(13):4298–4311
43. Kong Y, Huang L, Li W, Liu X, Zhou Y, Liu C, Zhang S, Xie F et al (2021) The synaptic vesicle protein 2A interacts with key pathogenic factors in Alzheimer's disease: implications for treatment. *Front Cell Dev Biol* 9:609908
44. Kong Y, Cao L, Xie F, Wang X, Zuo C, Shi K, Rominger A, Huang Q et al (2024) Reduced SV2A and GABAA receptor levels in the brains of type 2 diabetic rats revealed by [18F]SDM-8 and [18F]flumazenil PET. *Biomed Pharmacother*. 172:116252
45. Kreimerman I, Reyes AL, Paolino A, Pardo T, Porcal W, Ibarra M, Oliver P, Savio E et al (2019) Biological assessment of a (18)F-labeled sulforhodamine 101 in a mouse model of Alzheimer's disease as a potential astrocytosis marker. *Front Neurosci* 13:734
46. Kreisler WC, Kim MJ, Coughlin JM, Henter ID, Owen DR, Innis RB (2020) PET imaging of neuroinflammation in neurological disorders. *Lancet Neurol* 19(11):940–950
47. Li XY, Men WW, Zhu H, Lei JF, Zuo FX, Wang ZJ, Zhu ZH, Bao XJ et al (2016) Age- and brain region-specific changes of glucose metabolic disorder, learning, and memory dysfunction in early Alzheimer's disease assessed in APP/PS1 transgenic mice using (18)F-FDG-PET. *Int J Mol Sci* 17(10):1707
48. Liu B, Le KX, Park MA, Wang S, Belanger AP, Dubey S, Frost JL, Holton P et al (2015) In vivo detection of age- and disease-related increases in neuroinflammation by 18F-GE180 TSP0 microPET imaging in wild-type and Alzheimer's transgenic mice. *J Neurosci* 35(47):15716–15730
49. Liu Y, Zhu L, Plössl K, Choi SR, Qiao H, Sun X, Li S, Zha Z et al (2010) Optimization of automated radiosynthesis of [18F]AV-45: a new PET imaging agent for Alzheimer's disease. *Nucl Med Biol* 37(8):917–925
50. López-Picón FR, Keller T, Bocanea D, Helin JS, Krzyczmonik A, Helin S, Damont A, Dollé F et al (2022) Direct comparison of [(18)F]F-DPA with [(18)F]DPA-714 and [(11)C]PBR28 for neuroinflammation imaging in the same Alzheimer's disease model mice and healthy controls. *Mol Imaging Biol* 24(1):157–166
51. Marutle A, Gillberg P-G, Bergfors A, Yu W, Ni R, Nennesmo I, Voytenko L, Nordberg A (2013) 3 H-Deprenyl and 3 H-PIB autoradiography show different laminar distributions of astroglia and fibrillar β -amyloid in Alzheimer brain. *J Neuroinflammation* 10(1):1–15
52. Metaxas A, Thygesen C, Kempf SJ, Anzalone M, Vaitheeswaran R, Petersen S, Landau AM, Audrain H et al (2019) Ageing and amyloidosis underlie the molecular and pathological alterations of tau in a mouse model of familial Alzheimer's disease. *Sci Rep* 9(1):15758
53. Nam M-H, Ko HY, Kim D, Lee S, Park YM, Hyeon SJ, Won W, Chung J-I et al (2023) Visualizing reactive astrocyte-neuron interaction in Alzheimer's disease using 11C-acetate and 18F-FDG. *Brain* 146(7):2957–2974
54. Ni R, Gillberg P-G, Bogdanovic N, Viitanen M, Myllykangas L, Nennesmo I, Långström B, Nordberg A (2017) Amyloid tracers binding sites in autosomal dominant and sporadic Alzheimer's disease. *Alzheimers Dement* 13(4):419–430
55. Ni R, Gillberg PG, Bergfors A, Marutle A, Nordberg A (2013) Amyloid tracers detect multiple binding sites in Alzheimer's disease brain tissue. *Brain* 136(7):2217–2227
56. Ni R, Ji B, Ono M, Sahara N, Zhang MR, Aoki I, Nordberg A, Sahara T et al (2018) Comparative in vitro and in vivo quantifications of pathologic tau deposits and their association with neurodegeneration in tauopathy mouse models. *J Nucl Med* 59(6):960–966
57. Ni R, Rödner J, Voytenko L, Dyrks T, Thiele A, Marutle A, Nordberg A (2021) In vitro characterization of the regional binding distribution of amyloid PET tracer florbetaben and the glia tracers deprenyl and PK11195 in autopsy Alzheimer's brain tissue. *J Alzheimers Dis* 80(4):1723–1737
58. Nicholson RM, Kusne Y, Nowak LA, LaFerla FM, Reiman EM, Valla J (2010) Regional cerebral glucose uptake in the 3xTG model of Alzheimer's disease highlights common regional vulnerability across AD mouse models. *Brain Res* 1347:179–185
59. Oddo S, Caccamo A, Shepherd JD, Murphy MP, Golde TE, Kaye R, Metherate R, Mattson MP et al (2003) Triple-transgenic model of Alzheimer's disease with plaques and tangles: intracellular A β and synaptic dysfunction. *Neuron* 39(3):409–421
60. Olsen M, Aguilar X, Sehlin D, Fang XT, Antoni G, Erlandsson A, Syvänen S (2018) Astroglial responses to amyloid-beta progression in a mouse model of Alzheimer's disease. *Mol Imaging Biol* 20(4):605–614
61. Ono M, Sahara N, Kumata K, Ji B, Ni R, Koga S, Dickson DW, Trojanowski JQ et al (2017) Distinct binding of PET ligands PBB3 and AV-1451 to tau fibril strains in neurodegenerative tauopathies. *Brain* 140(3):764–780
62. Park BN, Kim JH, Lim TS, Park SH, Kim TG, Yoon BS, Son KS, Yoon JK et al (2020) Therapeutic effect of mesenchymal stem cells in an animal model of Alzheimer's disease evaluated by β -amyloid positron emission tomography imaging. *Aust N Z J Psychiatry* 54(9):883–891
63. Park JH, Ju YH, Choi JW, Song HJ, Jang BK, Woo J, Chun H, Kim HJ et al (2019) Newly developed reversible MAO-B inhibitor circumvents the shortcomings of irreversible inhibitors in Alzheimer's disease. *Sci Adv* 5(3):eaav0316
64. Poisnel G, Dhilly M, Moustié O, Delamare J, Abbas A, Guilloteau D, Barré L (2012) PET imaging with [18F]AV-45 in an APP/PS1-21 murine model of amyloid plaque deposition. *Neurobiol Aging* 33(11):2561–2571
65. Poisnel G, Hérard AS, El Tannir El Tayara N, Bourrin E, Volk A, Kober F, Delatour B, Delzescaux T et al (2012) Increased regional cerebral glucose uptake in an APP/PS1 model of Alzheimer's disease. *Neurobiol Aging* 33(9):1995–2005
66. Rodriguez-Vieitez E, Ni R, Gulyás B, Tóth M, Häggkvist J, Hallidin C, Voytenko L, Marutle A et al (2015) Astrocytosis precedes amyloid plaque deposition in Alzheimer APPswe transgenic mouse brain: a correlative positron emission tomography and in vitro imaging study. *Eur J Nucl Med Mol Imaging* 42(7):1119–1132
67. Rodriguez-Vieitez E, Saint-Aubert L, Carter SF, Almkvist O, Farid K, Schöll M, Chiotis K, Thordardottir S et al (2016) Diverging longitudinal changes in astrocytosis and amyloid PET in autosomal dominant Alzheimer's disease. *Brain* 139(Pt 3):922–936
68. Sancheti H, Akopian G, Yin F, Brinton RD, Walsh JP, Cadenas E (2013) Age-dependent modulation of synaptic plasticity and insulin mimetic effect of liponic acid on a mouse model of Alzheimer's disease. *PLoS One* 8(7):e69830
69. Santillo AF, Gambini JP, Lannfelt L, Långström B, Ulla-Marja L, Kilander L, Engler H (2011) In vivo imaging of astrocytosis

- in Alzheimer's disease: an 11C-L-deuteriodeprenyl and PIB PET study. *Eur J Nucl Med Mol Imaging* 38(12):2202–2208
70. Schedin-Weiss S, Inoue M, Hromadkova L, Teranishi Y, Yamamoto NG, Wiehager B, Bogdanovic N, Winblad B et al (2017) Monoamine oxidase B is elevated in Alzheimer disease neurons, is associated with γ -secretase and regulates neuronal amyloid β -peptide levels. *Alzheimers Res Ther* 9(1):57
 71. Serrano-Pozo A, Mielke ML, Gómez-Isla T, Betensky RA, Growdon JH, Frosch MP, Hyman BT (2011) Reactive glia not only associates with plaques but also parallels tangles in Alzheimer's disease. *Am J Pathol* 179(3):1373–1384
 72. Smit T, Deshayes NAC, Borchelt DR, Kamphuis W, Middeldorp J, Hol EM (2021) Reactive astrocytes as treatment targets in Alzheimer's disease-Systematic review of studies using the APPswePS1dE9 mouse model. *Glia* 69(8):1852–1881
 73. Snellman A, López-Picón FR, Rokka J, Salmona M, Forloni G, Scheinin M, Solin O, Rinne JO et al (2013) Longitudinal amyloid imaging in mouse brain with 11C-PIB: comparison of APP23, Tg2576, and APPswe-PS1dE9 mouse models of Alzheimer disease. *J Nucl Med* 54(8):1434–1441
 74. Snellman A, Takkinen JS, López-Picón FR, Eskola O, Solin O, Rinne JO, Haaparanta-Solin M (2019) Effect of genotype and age on cerebral [18F]FDG uptake varies between transgenic APPswe-PS1dE9 and Tg2576 mouse models of Alzheimer's disease. *Sci Rep* 9(1):5700
 75. Sérrière S, Tauber C, Vercouillie J, Mothes C, Pruckner C, Guilleaume D, Kassiou M, Doméné A et al (2015) Amyloid load and translocator protein 18 kDa in APPswePS1-dE9 mice: a longitudinal study. *Neurobiol Aging* 36(4):1639–52
 76. Tagai K, Ono M, Kubota M, Kitamura S, Takahata K, Seki C, Takado Y, Shinotoh H et al (2021) High-contrast in vivo imaging of tau pathologies in Alzheimer's and non-Alzheimer's disease tauopathies. *Neuron* 109(1):42–58.e8
 77. Tong J, Meyer JH, Furukawa Y, Boileau I, Chang LJ, Wilson AA, Houle S, Kish SJ (2013) Distribution of monoamine oxidase proteins in human brain: implications for brain imaging studies. *J Cereb Blood Flow Metab* 33(6):863–871
 78. Tournier BB, Tsartsalis S, Rigaud D, Fossey C, Cailly T, Fabis F, Pham T, Grégoire MC et al (2019) TSPO and amyloid deposits in sub-regions of the hippocampus in the 3xTgAD mouse model of Alzheimer's disease. *Neurobiol Dis* 121:95–105
 79. Venetis S, Lopresti BJ, Wang G, Hamilton RL, Mathis CA, Klunk WE, Apte UM, Wiley CA (2009) PK11195 labels activated microglia in Alzheimer's disease and in vivo in a mouse model using PET. *Neurobiol Aging* 30(8):1217–1226
 80. Verkhratsky A, Nedergaard M (2018) Physiology of Astroglia. *Physiol Rev* 98(1):239–389
 81. Vilaplana E, Rodriguez-Vieitez E, Ferreira D, Montal V, Almkvist O, Wall A, Lleó A, Westman E et al (2020) Cortical microstructural correlates of astrocytosis in autosomal-dominant Alzheimer disease. *Neurology* 94(19):e2026–e2036
 82. Villemagne VL, Harada R, Dore V, Furumoto S, Mulligan R, Kudo Y, Burnham S, Krishnadas N et al (2022) Assessing reactive astrogliosis with (18)F-SMBT-1 across the Alzheimer's disease spectrum. *J Nucl Med* 63(10):1560–1569
 83. Villemagne VL, Harada R, Doré V, Furumoto S, Mulligan R, Kudo Y, Burnham S, Krishnadas N (2022) First-in-humans evaluation of (18)F-SMBT-1, a novel (18)F-labeled monoamine oxidase-B PET tracer for imaging reactive astrogliosis. *J Nucl Med* 63(10):1551–1559
 84. Waldron AM, Wintmolders C, Bittelbergs A, Kelley JB, Schmidt ME, Stroobants S, Langlois X, Staelens S (2015) In vivo molecular neuroimaging of glucose utilization and its association with fibrillar amyloid- β load in aged APPPS1-21 mice. *Alzheimers Res Ther* 7(1):76
 85. Weng CC, Hsiao IT, Yang QF, Yao CH, Tai CY, Wu MF, Yen TC, Jang MK et al (2020) Characterization of (18)F-PM-PBB3 ((18)F-APN-1607) Uptake in the rTg4510 mouse model of tauopathy. *Molecules* 25(7):1750
 86. Wilson A, Garcia A, Chestakova A, Kung H, Houle S (2004) A rapid one-step radiosynthesis of the β -amyloid imaging radiotracer N-methyl-[11C]2-(4'-methylaminophenyl)-6-hydroxybenzothiazole ([11C]-6-OH-BTA-1). *J Label Compd Radiopharm* 47:679–682
 87. Zhou R, Ji B, Kong Y, Qin L, Ren W, Guan Y, Ni R (2021) PET imaging of neuroinflammation in Alzheimer's disease. *Front Immunol* 12:739130

Publisher's Note Springer Nature remains neutral with regard to jurisdictional claims in published maps and institutional affiliations.